Chemical Science

ROYAL SOCIETY OF CHEMISTRY

EDGE ARTICLE

View Article Online
View Journal

Cite this: DOI: 10.1039/d5sc08142d

All publication charges for this article have been paid for by the Royal Society of Chemistry

High-yield synthesis of graphene quantum dots from spent graphite and application in hydrogel Zn batteries

Dingzhong Luo, Yinger Xiang, Zhenglei Geng, Huaxin Liu, Xue Zhong, Zhi Zheng, Zhiyu Hu, Shengli Lu, Wentao Deng, Guoqiang Zou, Hongshuai Hou * and Xiaobo Ji

With the widespread development of electric vehicles, the number of spent lithium-ion batteries (LIBs) is steadily increasing each year. Meanwhile, the spent graphite anode, with low regeneration value and significant environmental impact, has emerged as an increasingly concerning issue. In this study, we adequately utilize the characteristic features of spent graphite, such as large interlayer spacing, abundant defects and a broken crystal structure resulting from repeated charge–discharge cycles, to fabricate uniform and single-layer graphene quantum dots (GQDs). Even more impressively, the yield of spent graphite derived GQDs is as high as 61.3%, which is much higher than that of GQDs from pristine graphite (11.8%). These GQDs with abundant hydrophilic functional groups are anchored onto a polyvinyl alcohol (PVA) matrix to construct a composite hydrogel electrolyte (0.8GQDs@PVA@Zn). When employed in zinc-ion batteries, ultra-stable cycling for 5500 h in Zn||Zn symmetric cells and 9000 cycles in Zn||Cu half-cells is realized. The outstanding battery performance can be attributed to the ability of GQDs to enhance the mechanical properties of the hydrogel electrolyte, regulate the composition and distribution of the solid electrolyte interphase, and modify the Zn^{2+} flux. This work offers a high-value recycling strategy for graphite anodes from spent LIBs.

Received 21st October 2025
Accepted 7th December 2025

DOI: 10.1039/d5sc08142d

rsc.li/chemical-science

Introduction

In recent years, electric vehicles have developed rapidly, and the number of retired lithium-ion batteries from electric vehicles is expected to surge.[1] Efficient recycling of these batteries, preventing environmental contamination while recovering valuable components, has become increasingly significant.[2] However, since the graphite anode materials of spent lithium-ion batteries do not contain the precious metals found in the cathode and their structure is severely degraded, making it difficult to regenerate battery-grade graphite, the recycling and regeneration of these materials into battery-grade graphite is both challenging and economically unfeasible.[3–5] Furthermore, toxic organic electrolytes and binders remain within the material after disassembly, necessitating proper disposal to avoid environmental hazards.[6,7] Therefore, it is essential to explore alternative approaches that leverage the inherent characteristics of spent graphite for high-value transformation, rather than simply regenerating it as battery-grade graphite or utilizing it for low-value applications such as adsorbents, fillers, or reductants.[8]

GQDs have garnered significant attention in both theoretical[9,10] and applied research fields due to their quantum size effects, abundant functional groups, photoluminescence properties, and low toxicity.[11,12] These characteristics make them promising candidates for applications such as bioimaging,[13] therapy,[14] catalysis,[15] and electrochemical energy storage.[16] However, one of the primary obstacles to the large-scale application of GQDs lies in their high production costs.[17] The synthesis of GQDs is generally categorized into two approaches: the top-down method and the bottom-up method.[18] The bottom-up approach relies on expensive organic molecular precursors and involves complex and stringent reaction conditions,[19,20] whereas the top-down approach uses abundant and cost-effective carbon-based precursors, offering a more economical solution with greater scalability.[21] However, GQDs produced through the top-down method often suffer from poor size uniformity, low yields, and difficulties in obtaining single-layer GQDs.[22] These limitations are primarily attributed to the challenges of uniformly oxidizing and cutting bulk carbon materials with tightly packed graphitized structures into graphene quantum dots smaller than 10 nm.[22,23] The ability to produce GQDs with uniform size and high yield often signifies improved product quality and reduced production costs. Moreover, single-layer GQDs, owing to their larger specific surface area, can expose more functional groups and exhibit

College of Chemistry and Chemical Engineering, Central South University, Changsha, 410083, China. E-mail: hs-hou@csu.edu.cn

more reactive physicochemical properties compared to multi-layer GQDs.[24] Therefore, investigating strategies to overcome the limitations of top-down approaches for the fabrication of uniform-sized, high-yield, and single-layer GQDs is of great significance.

Interestingly, spent graphite from LIBs offers a unique advantage in overcoming these limitations. Graphite electrodes derived from spent LIBs undergo significant structural changes due to the repeated intercalation and deintercalation of lithium ions during charge–discharge cycles.[25] These processes lead to an increased lattice spacing and the disruption of the long-range ordered and tightly packed graphitic structure, resulting in a material that is rich in lattice defects.[8] While these defects are detrimental to the graphite's performance in battery systems and contribute to capacity degradation,[26] they present a unique advantage for the top-down oxidation and cutting processes required to produce small-sized GQDs. These structural characteristics are expected to improve both the yield and size uniformity of GQDs synthesized *via* the top-down approach.

Aqueous zinc-ion batteries (ZIBs) have been considered potential alternatives for next-generation energy storage systems owing to their low cost, high safety, non-flammability, and simple operational conditions.[27] However, the zinc anode suffers from several critical issues, such as dendrite growth, zinc corrosion, and the formation of side products, which significantly limit the commercialization of ZIBs.[28] Electrolyte modification is generally considered as one of the effective solutions to these problems. GQDs with abundant hydrophilic functional groups have shown great promise as electrolyte additives in aqueous batteries.[29] However, when GQDs are used as additives in liquid electrolyte systems, their role is generally limited to co-deposition or electrostatic shielding.[30] Hydrogel electrolytes, as quasi-solid-state electrolytes with hydrophilic polymer frameworks, not only exhibit superior mechanical properties compared to liquid electrolyte systems but also have hydrophilic functional groups on the polymer chains that mitigate side reactions between water molecules and the zinc anode.[31,32] Nonetheless, the mechanical strength of conventional hydrogels is insufficient to support safe application under external stresses, and repeated folding or stretching can lead to deformation or cracking.[33] Although the hydrophilic groups in the polymer chains can suppress the activity of water molecules, some free water remains, posing challenges related to water electrolysis and the crystallization of water at low temperatures, which reduces ion conductivity.[34,35] Modification of hydrogels with carbon-dots-based nanomaterials has been demonstrated as an effective approach to enhance the mechanical properties of hydrogels.[36] Nevertheless, the modification of hydrogel electrolytes for ZIBs using GQDs to improve both their mechanical and electrochemical performance remains a promising area of exploration.

In this study, GQDs with a uniform size and single-layer structure were synthesized from graphite electrodes of retired lithium-ion batteries. Thanks to the unique structure of the spent graphite electrode, such as large layer spacing, abundant defects, and broken crystal structure, the yield of GQDs is nearly 5 times higher than that of pristine graphite. The obtained GQDs, rich in carboxyl groups, were then esterified with the hydrophilic polymer polyvinyl alcohol (PVA) to form a strong network structure within the polymer framework, resulting in a hydrogel electrolyte with excellent mechanical and electrochemical properties for zinc-ion batteries. The Zn‖Zn symmetric cells and Zn‖Cu half-cells using the 0.8GQDs@PVA@Zn hydrogel electrolyte exhibited outstanding stability, operating for over 5500 hours and 9000 cycles, respectively. The assembled pouch cells not only maintained normal operation at low temperatures but also continued to deliver power under extreme mechanical stress. Studies on the solid-electrolyte interphase (SEIs) of the zinc anode revealed that the modification of the hydrogel electrolyte with GQDs not only suppressed undesirable side reactions between water molecules and the zinc anode but also inhibited the decomposition of $CF_3SO_3^-$ in the electrolyte, thereby regulating the composition and distribution of the SEI film. Observations of zinc nucleation and theoretical calculations indicated that GQDs anchored on the PVA framework could homogenize the electric field distribution and alter the original zinc ion flux, thus promoting nucleation site formation and inhibiting dendrite growth. This work provides a high-value strategy for the recycling of spent graphite anodes from lithium-ion batteries and explores the potential applications of GQDs in hydrogel electrolytes for zinc-ion batteries.

Results and discussion

Recycling and high-quality, high-value transformation of spent graphite

As shown in Fig. 1a, the recycling and high-value conversion of spent graphite involves several steps, including the disassembly of the pouch cell and the separation of the anode powder from the current collector. The spent graphite is then subjected to oxidation and cutting using nitric acid and sulfuric acid, resulting in an acidified solution containing GQDs. Sodium carbonate is employed to neutralize the acid-containing solution, which yields a mixture containing GQDs and sodium sulfate. The neutralized solution is then heated and concentrated through evaporation, followed by cooling and standing, leading to the precipitation of a significant amount of hydrated sodium sulfate. After drying, sodium sulfate powder is obtained, which is confirmed by X-ray diffraction (XRD) to contain only Na_2SO_4, with no other impurity phases such as sodium nitrate (Fig. S1, SI). This is due to the complete reaction of nitric acid with the defective structure of the spent graphite, leaving no nitrate ions in the solution. The concentrated solution contains a high quantity of GQDs, which are subsequently separated and purified *via* dialysis and freeze-drying to yield GQD powder.

The XRD patterns of both spent graphite and GQDs are shown in Fig. S2 (SI). After acid oxidation, the diffraction peak of spent graphite at approximately 26.5° disappears, indicating that the structure of the spent graphite has been disrupted and successfully converted into GQDs.[37] The element valence distribution of GQDs was further analyzed by X-ray photoelectron spectroscopy (XPS) (Fig. S3, SI). The high-resolution C 1s

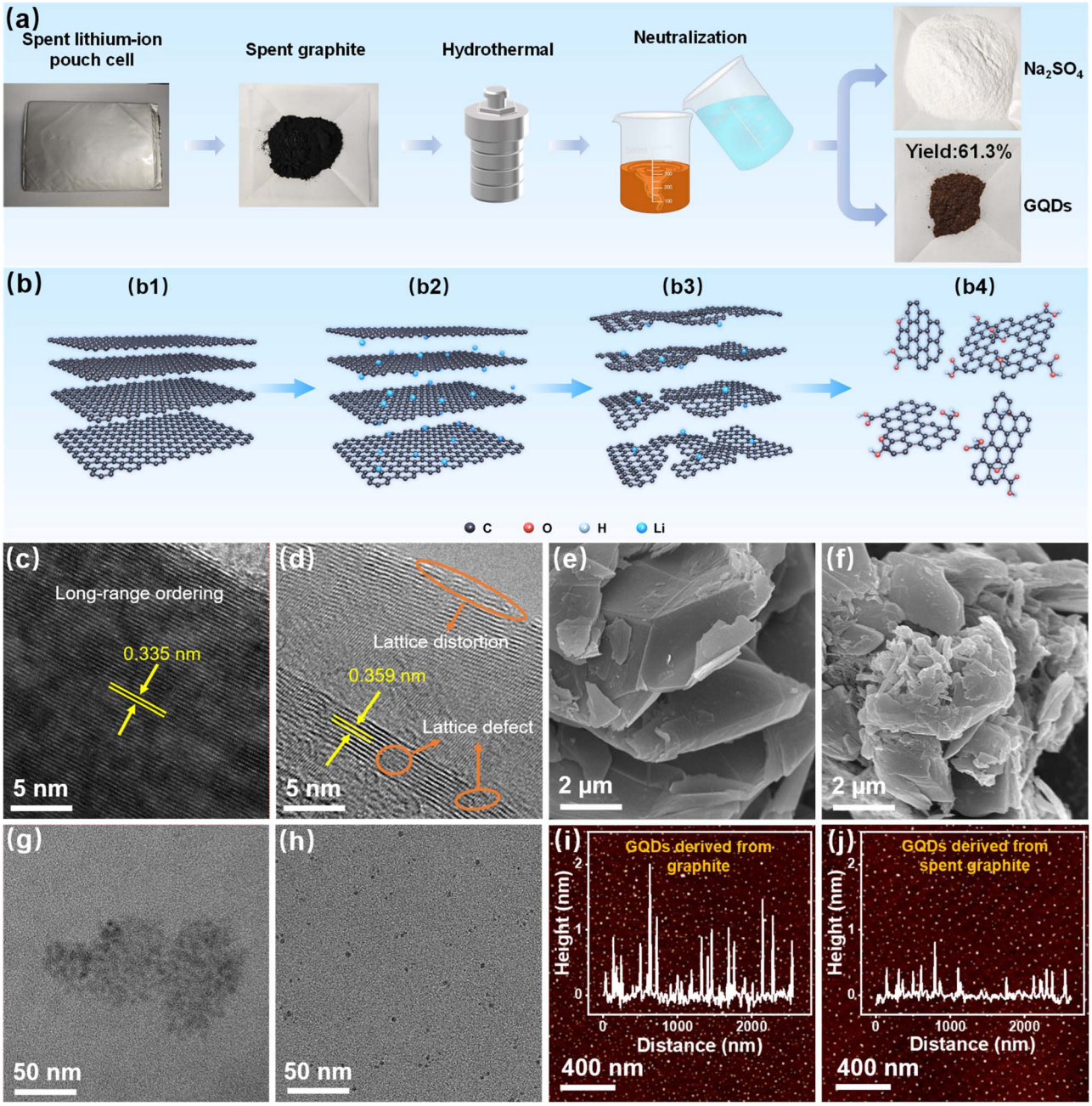

Fig. 1 Schematic diagram and characterization of high-value conversion of a spent graphite anode. (a) Flowchart illustrating the recycling and high-value conversion process of anode graphite from a spent lithium-ion pouch cell. (b) Schematic representation of the microstructural changes of anode graphite during charge/discharge cycles and the recycling process: (b1) graphite structure before cycling; (b2) graphite structure after lithium-ion insertion; (b3) spent graphite structure after multiple charge/discharge cycles; (b4) structure of the product after oxidation cutting with strong acid. HRTEM images of graphite (c) and spent graphite (d). SEM images of graphite (e) and spent graphite (f). TEM images of GQDs derived from graphite (g) and spent graphite (h). AFM images and corresponding height distribution of GQDs derived from graphite (i) and spent graphite (j).

spectrum (Fig. S4, SI) exhibits three distinct peaks at 284.8, 285.33, and 289.0 eV, corresponding to C=C, C–O, and O–C=O bonds, respectively.[23,38] Additionally, the O 1s XPS spectrum (Fig. S5, SI) shows three peaks at 532.1, 533.6, and 535.5 eV, attributed to O–C=O, C–O, and H_2O, respectively.[37,39] These XPS spectra indicate that the GQDs contain a rich array of oxygen-containing functional groups, such as hydroxyl and carboxyl groups. We weighed the GQDs obtained from the reaction of 1g of spent graphite and found that 613.08 mg of product was obtained (Fig. S6, SI), corresponding to a yield of 61.3%, which is significantly higher than the yield (11.8%) obtained using pristine graphite as the precursor (Fig. S7, SI). This enhanced yield is attributed to the unique structural changes that graphite undergoes when used as the anode in lithium-ion

batteries (Fig. 1b). The well-ordered long-range structure of graphite (Fig. 1b1) undergoes an increase in interlayer spacing due to the intercalation of lithium ions (Fig. 1b2). During repeated charge–discharge cycles in a lithium-ion battery, the intercalation and de-intercalation of lithium ions further exacerbate the expansion of the interlayer spacing and cause structural degradation, resulting in defects and distortions in the graphite lattice (Fig. 1b3).[26] These enlarged interlayer spacings, along with the lattice defects and distortions, facilitate the oxidation and cutting of graphite by nitric acid to form GQDs (Fig. 1b4), thereby leading to a high yield of GQDs.

To verify this process, we performed transmission electron microscopy (TEM) to observe the microstructure of both graphite and spent graphite. As shown in Fig. 1c, pristine graphite exhibits a well-ordered layered structure with an interlayer distance of 0.335 nm, consistent with the standard spacing of highly crystalline graphite. In contrast, the high-resolution TEM (HRTEM) image of spent graphite (Fig. 1d) reveals a noticeably enlarged interlayer spacing resulting from the repeated intercalation and de-intercalation of lithium ions. Moreover, spent graphite exhibits a substantially more disordered structure, with clear lattice distortions and defect-rich regions.

Importantly, these defects are not limited to the surface; instead, the disordered lattice fringes extend into the particle bulk, indicating pervasive internal degradation. This observation is consistent with prior studies on the structural evolution of graphite during cycling, which have shown that lithium intercalation can induce significant deformation of graphene layers and generate structural defects even at very early stages of cycling.[26] Although partial structural recovery may occur during delithiation, a portion of these defects remains, ultimately accumulating during long-term cycling. Therefore, the severely aged graphite harvested from end-of-life lithium-ion batteries inevitably contains abundant bulk defects and expanded interlayer spacing—structural features that greatly facilitate the oxidative cutting process in top-down GQD synthesis. Raman spectroscopy further corroborates this, showing that the D peak, attributed to disordered carbon at approximately 1348 cm^{-1}, is stronger in spent graphite compared to graphite, while the G peak corresponding to ordered graphite carbon is weaker (Fig. S8, SI). Scanning electron microscopy (SEM) images also reveal a more fragmented surface morphology of spent graphite compared to pristine graphite (Fig. 1e and f).

TEM analysis of GQDs derived from both graphite and spent graphite reveals that the GQDs derived from graphite typically have sizes ranging from 5 to 10 nm, while those derived from spent graphite have sizes between 2 and 4 nm (Fig. 1g and h, and S9a and b, SI). Therefore, GQDs produced from spent graphite not only have smaller sizes compared to those derived from graphite but also exhibit better size uniformity. Additionally, atomic force microscopy (AFM) was employed to compare the thickness of GQDs derived from both precursors. As shown in Fig. 1i, the GQDs obtained from graphite have a thickness ranging from 0.4 to 2.0 nm, corresponding to 1–6 layers of graphene, with most GQDs being 2–4 layers thick. In contrast, the GQDs derived from spent graphite have a thickness ranging from 0.4 to 0.7 nm, corresponding to 1–2 layers of graphene, with the majority being single-layer graphene quantum dots (Fig. 1j). Therefore, by using spent graphite as a precursor, it is possible to produce high-quality, monolayer GQDs with uniform size, which contrasts with the traditional approach of using pristine graphite.

Subsequently, the optical properties of GQDs were characterized. As shown in Fig. S10 (SI), the UV-vis absorption spectrum displays three distinct absorption bands, corresponding to the π–π^* transition of C–C bonds of the carbon core, the π–π^* transition of sp^2 carbon at edge charge-transfer sites, and the n–π^* transition associated with surface states of oxygen-containing functional groups.[40] Photoluminescence excitation (PLE) measurements of GQDs reveal a peak with maximum intensity at approximately 340 nm, while under 340 nm excitation, the photoluminescence (PL) emission spectrum exhibits a maximum intensity emission peak at 470 nm (Fig. S11, SI). As illustrated in Fig. S12 (SI), the excitation-wavelength-dependent PL behavior indicates the existence of several emission centers.

Characterization of GQD-crosslinked hydrogel electrolytes

Due to the top-down method involving the oxidation and cutting of spent graphite with strong acids, the resulting GQDs contain a significant amount of carboxyl groups. To achieve chemical crosslinking of PVA, we first exploit the abundant carboxyl groups on the GQDs to react with the hydroxyl groups on the PVA side chains, forming ester bonds. The chemical crosslinking between GQDs and PVA is depicted in Fig. 2a. Subsequently, PVA is dissolved in a mixed solvent of water and dimethyl sulfoxide (DMSO) through heating and then subjected to cyclic freeze–thawing. This process enhances hydrogen bonding between PVA chains *via* the co-nonsolvency effect[41] among PVA, water, and DMSO, thereby creating robust physical crosslinks. The chemically and physically dual-crosslinked hydrogel is then immersed in an electrolyte containing zinc salts to form the hydrogel electrolyte, with the specific experimental steps outlined in the methods.

After freeze-drying the prepared hydrogel, we used liquid nitrogen fracturing to obtain cross-sectional SEM images (Fig. 2b and d), which revealed that both the bare hydrogel and the hydrogel containing GQDs feature abundant interconnected three-dimensional pores. This porous structure is highly conducive to zinc ion diffusion. However, the SEM images at higher magnification (Fig. 2c and e) show that the pores in the GQD-containing hydrogel are smaller compared to those in the bare hydrogel. This reduction in pore size is due to the formation of ester bonds between GQDs and PVA chains, which shortens the distance between PVA chains, resulting in smaller pores. In zinc-ion batteries, hydrogels with smaller pore sizes typically exhibit superior mechanical properties, which are more effective in suppressing dendrite growth.[42]

To confirm the formation of ester bonds between PVA and GQDs, we performed Fourier transform infrared (FTIR) spectroscopy on bare PVA and GQD-crosslinked PVA (0.8GQDs@PVA). As shown in Fig. 2f, the absorption band at 1620 cm^{-1} indicates the presence of carboxyl groups in GQDs.[37]

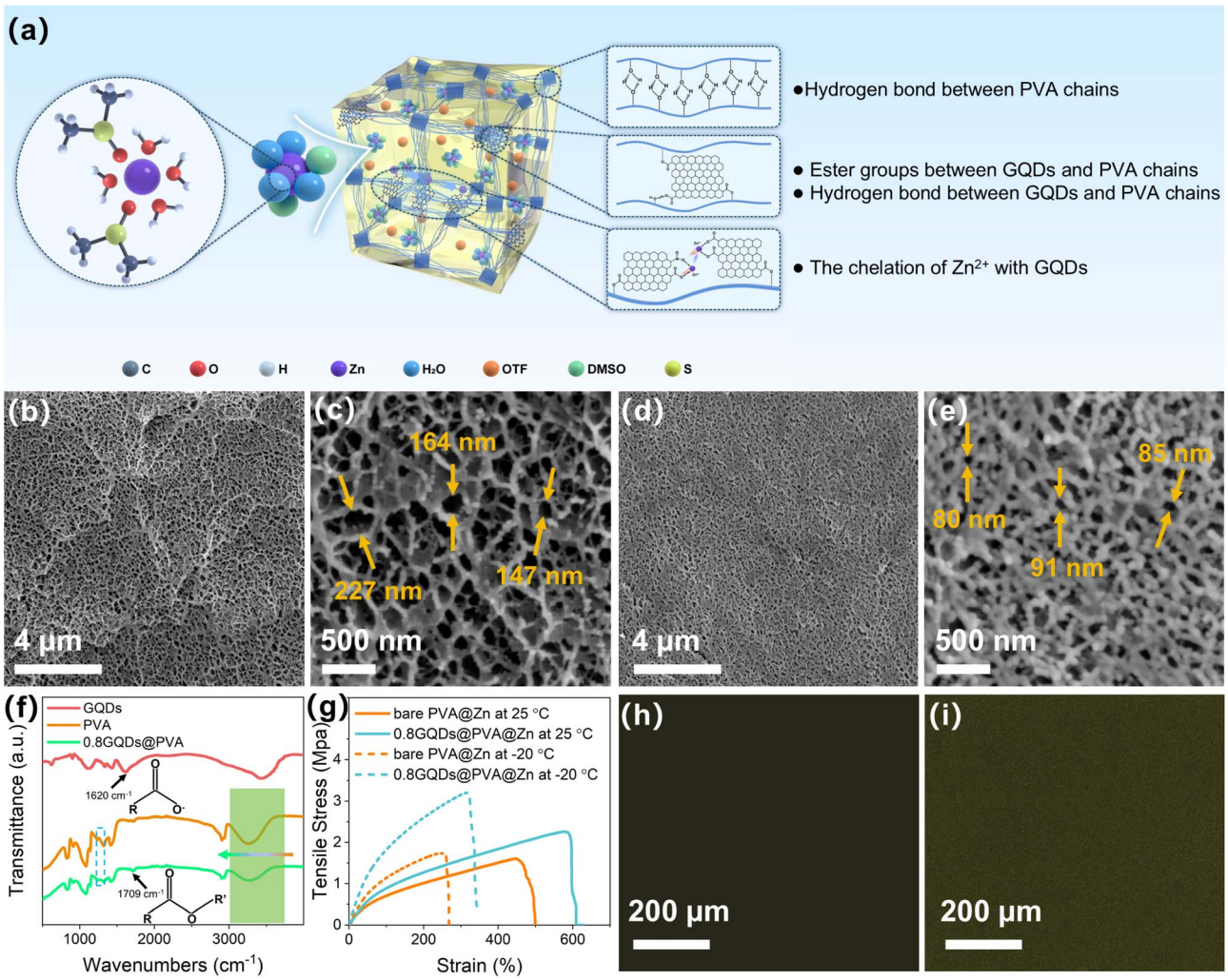

Fig. 2 Schematic diagram and characterization of GQD-modified hydrogel electrolyte. (a) Schematic illustration of the internal hydrogen bonding, ester groups, and interactions between zinc ions and GQDs within the GQD-modified hydrogel electrolyte. (b) Cross-sectional SEM image of bare PVA. (c) Corresponding local magnified view of (b). (d) Cross-sectional SEM image of 0.8GQDs@PVA. (e) Corresponding local magnified view of (d). (f) FTIR spectroscopy of GQDs, PVA, and 0.8GQDs@PVA. (g) Tensile test results of bare PVA@Zn and 0.8GQDs@PVA@Zn at 25 °C and −20 °C. Fluorescence image of bare PVA@Zn (h) and 0.8GQDs@PVA@Zn (i).

In the 0.8GQDs@PVA sample, the stretching vibration peak corresponding to the carboxyl group becomes significantly weaker, while a new absorption band at 1709 cm^{-1} appears, which is attributed to the C=O bond in the ester group.[43,44] Although a similar C=O stretching vibration peak is observed at 1709 cm^{-1} in bare PVA, this originates from ester groups in the residual side chains of unhydrolyzed PVA (PVA1799).[44] The peak in pure PVA is weaker than that in 0.8GQDs@PVA because the esterification degree is lower in the absence of GQDs. Additionally, ester groups typically exhibit an absorption band around 1270 cm^{-1} corresponding to the C–O–C stretch.[45] A detailed analysis of the FTIR spectra (Fig. S13, SI) reveals an absorption peak at 1267 cm^{-1} in 0.8GQDs@PVA, which is absent in bare PVA, further confirming the formation of ester bonds between GQDs and PVA. The introduction of ester groups generally leads to a reduction in the number of hydroxyl groups on the PVA chain, which in turn diminishes intermolecular or intramolecular hydrogen bonding. This results in an increase in the vibrational frequency of the O–H bond around 3260 cm^{-1}, causing the corresponding absorption peak to shift to higher wavenumbers.[46] However, the esterification between GQDs and PVA chains leads to the formation of a new hydrogen bond network involving the C=O group, which restricts the O–H bond vibrations, lowering the vibration frequency. Moreover, the oxygen-containing functional groups (*e.g.*, hydroxyl, carboxyl, or epoxy groups) on the surface of the GQDs can form strong hydrogen bonds with the hydroxyl groups on PVA, further decreasing the O–H vibration frequency.[47] As shown in Fig. 2f (right), the O–H absorption peak of 0.8GQDs@PVA shifts slightly to lower wavenumbers compared to bare PVA.

To verify the stability of GQDs fixed onto PVA chains through esterification, we immersed the 0.8GQDs@PVA hydrogel membrane in electrolyte and observed whether the GQDs would detach from the PVA matrix. As shown in Fig. S14 (SI), the PVA

hydrogel containing GQDs maintained a light yellow color even after being immersed in the electrolyte for 1, 2, 3, and 6 days, indicating the stability of GQDs in the PVA matrix. If the GQDs were not fixed on the PVA chains, their excellent water solubility would cause them to diffuse rapidly through the three-dimensional pores of the hydrogel into the electrolyte, resulting in a color change of the hydrogel membrane. Therefore, the GQDs in the 0.8GQDs@PVA hydrogel membrane remain stably fixed in the PVA matrix *via* chemical bonds in the zinc salt-containing electrolyte. The 0.8GQDs@PVA hydrogel electrolyte, after being immersed in the zinc salt electrolyte for 6 days, is designated as 0.8GQDs@PVA@Zn, while the pure PVA hydrogel electrolyte is referred to as bare PVA@Zn. Mechanical performance tests of 0.8GQDs@PVA@Zn and bare PVA@Zn (Fig. 2g) show that 0.8GQDs@PVA@Zn exhibits superior tensile strength at both room temperature (25 °C) and −20 °C, compared to bare PVA@Zn. The enhanced mechanical properties of 0.8GQDs@PVA@Zn, due to the additional chemical crosslinking network formed by GQDs and PVA, suggest improved resistance to dendrite puncture in ZIBs. Confocal fluorescence imaging of 0.8GQDs@PVA@Zn and bare PVA@Zn (Fig. 2h and i) reveals no fluorescence signal in the bare PVA@Zn sample, while a uniform fluorescence signal is observed in the 0.8GQDs@PVA@Zn sample, confirming that GQDs are evenly fixed onto the PVA chains.

To evaluate the zinc ion conductivity of 0.8GQDs@PVA@Zn, we performed ion conductivity tests. The thickness of the hydrogel was controlled at approximately 215 μm (Fig. S15, SI). Electrochemical impedance spectroscopy (EIS) was used to measure the ion conductivity of both 0.8GQDs@PVA@Zn and bare PVA@Zn, yielding an ion conductivity of 2.59 mS cm^{-1} for 0.8GQDs@PVA@Zn, which is significantly higher than the 0.199 mS cm^{-1} for bare PVA@Zn (Fig. S16, SI). The enhanced ion conductivity of 0.8GQDs@PVA@Zn is attributed to the coordination effect of carboxyl groups on the GQDs with zinc ions, enabling zinc ion transport not only through the hydrogel's pores but also along the PVA side chains fixed with GQDs. Additionally, due to the strong hygroscopicity of GQDs, 0.8GQDs@PVA@Zn exhibits superior moisture retention compared to bare PVA@Zn (Fig. S17, SI), ensuring stable battery operation in high-temperature and dry environments. Furthermore, to ensure stable operation of the ZIBs at low temperatures, the antifreeze performance of the hydrogel is crucial. Differential scanning calorimetry (DSC) analysis reveals an exothermic peak around 0 °C for bare PVA@Zn (Fig. S18a, SI), indicating the presence of water molecules that can freeze in the bare hydrogel electrolyte. In contrast, no exothermic peak is observed in 0.8GQDs@PVA@Zn even at temperatures as low as −70 °C (Fig. S18b, SI), demonstrating that the inclusion of GQDs disrupts the continuous hydrogen bonding network between water molecules, preventing their freezing and significantly enhancing the antifreeze performance of the system.

Performance of zinc ion batteries with GQD-modified hydrogel electrolytes

In order to investigate the potential of GQD-modified hydrogel electrolytes in enhancing the cycling stability of zinc anodes, hydrogels with varying concentrations of GQDs were prepared and their electrochemical performance was evaluated in Zn‖Zn symmetric cells. As shown in Fig. 3a, at a current density of 1 mA cm^{-2}, hydrogels modified with GQD concentrations of 0.4, 0.8, and 1.2 g L^{-1} exhibited improved long-cycle performance compared to bare PVA@Zn electrolytes. Moreover, a clear trend in performance was observed: the cycling stability of the Zn‖Zn symmetric cells initially increased with GQD concentration, peaking at 0.8 g L^{-1}, which achieved stable operation for over 5500 hours. Additionally, the polarization voltage decreased with the GQD concentration, with values for bare PVA@Zn, 0.4GQDs@PVA@Zn, 0.8GQDs@PVA@Zn, and 1.2GQDs@PVA@Zn being 172, 155, 91, and 77 mV, respectively (Fig. S19, SI). To explore the reasons for the performance enhancement, Zn^{2+} transference number measurements were performed on the hydrogels modified with different GQD concentrations. As shown in Fig. S20 and 21 (SI), the Zn^{2+} transference numbers increased with the GQD concentration. The transference number for bare PVA@Zn was 0.184, which is slightly lower than that reported in the literature for aqueous ZIB electrolytes.[48] This can be attributed to the difficulty in Zn^{2+} migration caused by the large DMSO molecules within the hydrated Zn^{2+} structure. The hydrophilic groups on the GQDs, however, are capable of disrupting the solvent structure, while carboxyl groups (-COO^- and –OH) on GQDs can complex with Zn^{2+}, which are anchored within the PVA matrix. This results in the formation of additional migration channels for Zn^{2+} along the PVA chains, thus increasing the Zn^{2+} transference numbers. The transference numbers of 0.4GQDs@PVA@Zn, 0.8GQDs@PVA@Zn, and 1.2GQDs@PVA@Zn were measured to be 0.340, 0.418, and 0.455, respectively. Further stability tests at higher currents were performed on the 0.8GQDs@PVA@Zn symmetric cell, which showed a cycling lifetime of 4500 hours at 2.0 mA cm^{-2} (Fig. 3b), a significant improvement over the bare PVA@Zn electrolyte (550 hours). The 0.8GQDs@PVA@Zn hydrogel electrolyte prepared in this study exhibits excellent electrochemical performance, surpassing the values reported in previous studies (Fig. 3c).[49–59] This represents a significant advancement in the field of ZIB energy storage. At even higher current density and areal capacity (4 mA cm^{-2} and 4 mAh cm^{-2}), the 0.8GQDs@PVA@Zn symmetric cell exhibited superior cycling stability compared to bare PVA@Zn (Fig. S22, SI). The rate performance of the symmetric cells, shown in Fig. S23 (SI), demonstrates that 0.8GQDs@PVA@Zn maintains lower and more stable polarization voltages across current densities of 0.1, 0.3, 0.5, 1, 2, and 4 mA cm^{-2} compared to bare PVA@Zn. To verify the antifreeze properties of 0.8GQDs@PVA@Zn, symmetrical cells assembled with 0.8GQDs@PVA@Zn and bare PVA@Zn were cycled at −20 °C and −40 °C. As shown in Fig. S24 and 25 (SI), the cells using 0.8GQDs@PVA@Zn exhibited more stable cycling performance than those using bare PVA@Zn, in accordance with the excellent antifreeze properties observed in the DSC tests. Furthermore, chronopotentiometry measurements were conducted to explore the role of GQDs in guiding zinc nucleation (Fig. 3d). The nucleation overpotential (NOP), which reflects the energy barrier during the initial deposition process, was 78.7 mV for the bare PVA@Zn symmetric cell at

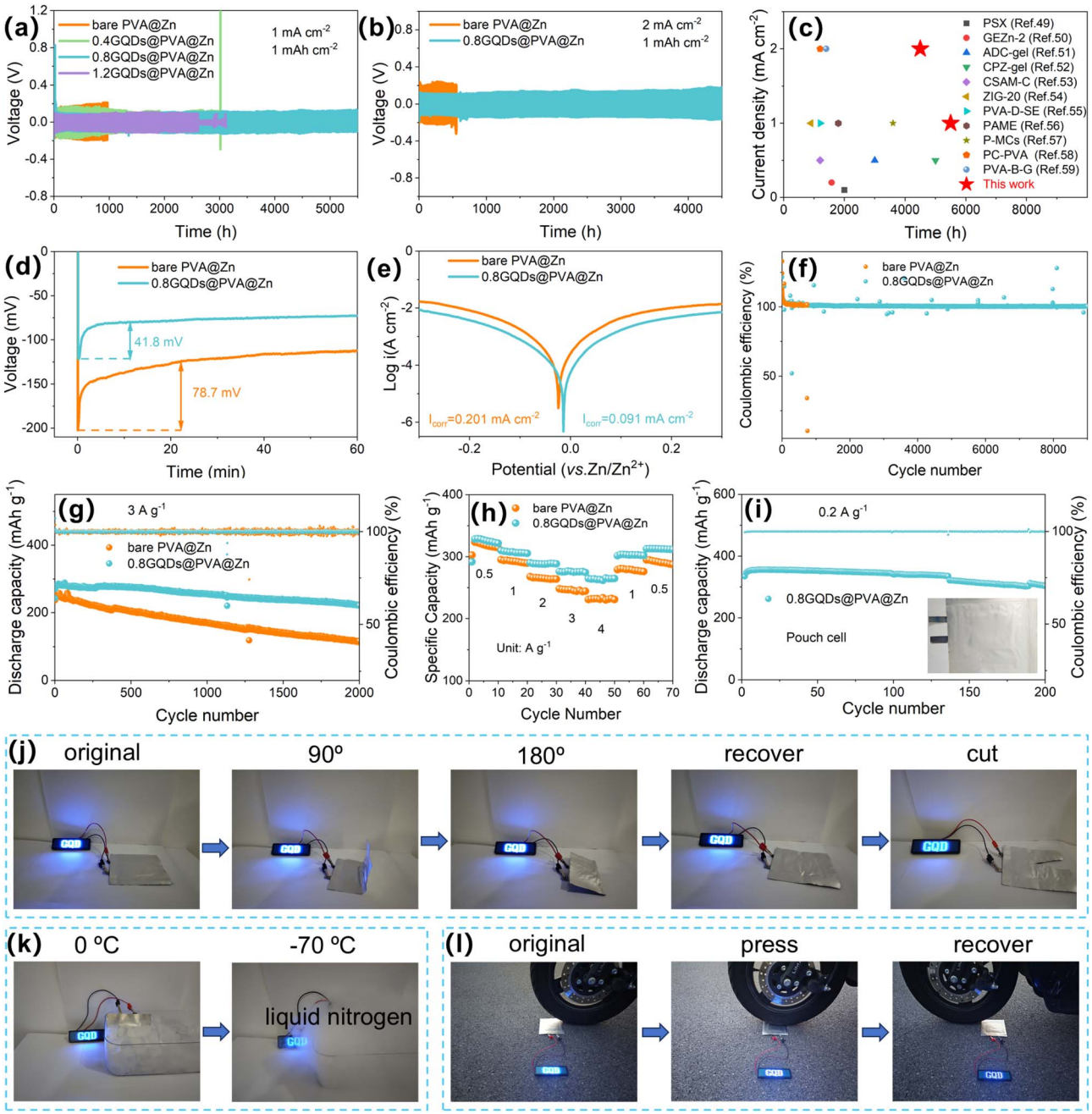

Fig. 3 Electrochemical performance of the GQD-modified hydrogel electrolyte. Cycling performance of Zn||Zn symmetric cells with bare PVA@Zn and 0.8GQDs@PVA@Zn at 1 mA cm^{-2} (a) and 2 mA cm^{-2} (b). (c) Comparison of the cycling properties of 0.8GQDs@PVA@Zn with those in other reports. (d) Nucleation overpotential curves for zinc nucleation. (e) Tafel curves of the Zn anode. (f) Coulombic efficiency of Zn||Cu batteries. (g) Cycling performance of Zn||NVO full cells at 3 A g^{-1}. (h) Rate capability at different current densities from 0.5 to 4 A g^{-1}. (i) Cycling performance of the Zn||NVO pouch cell using 0.8GQDs@PVA@Zn at 0.2 A g^{-1}. Photographs of the pouch cell using 0.8GQDs@PVA@Zn as the electrolyte, driving an LED light under bending, shearing (j), freezing (k), and compression (l) conditions.

1 mA cm^{-2}, whereas it decreased to 41.8 mV with the addition of GQDs to the PVA matrix. This reduction in NOP is attributed to the strong affinity of functional groups ($–COO^-$ and –COH) on GQDs with zinc ions, which lowers the nucleation barrier. Tafel curve analysis was performed to study the corrosion rate of the zinc anode in the hydrogel electrolytes. As shown in Fig. 3e, the corrosion current density for the zinc anode in 0.8GQDs@PVA@Zn was 0.091 mA cm^{-2}, compared to 0.201 mA cm^{-2} for bare PVA@Zn. The decrease in corrosion current suggests that the addition of GQDs reduces the hydrogen evolution rate, likely due to the hydrogen-bonding interactions between the oxygen-rich functional groups on GQDs and water molecules, which alleviates side reactions involving water. Linear sweep voltammetry (LSV) further demonstrated the enhanced

electrochemical stability window of 0.8GQDs@PVA@Zn (Fig. S26, SI). Compared to bare PVA@Zn, 0.8GQDs@PVA@Zn showed lower HER current responses, confirming its superior corrosion resistance. A lower OER current response further validated its overall electrochemical stability. These improvements are primarily attributed to the reduced free water content due to the water–GQD interactions. To evaluate the stability of Zn^{2+} plating/stripping cycles, Zn||Cu batteries with 0.8GQDs@PVA@Zn and bare PVA@Zn were tested for coulombic efficiency. As shown in Fig. 3f, the Zn||Cu battery with bare PVA@Zn exhibited unstable cycling efficiency, with rapid decay after 733 cycles. In contrast, the Zn||Cu battery employing the 0.8GQDs@PVA@Zn hydrogel electrolyte achieved an ultralong cycle life of 9000 cycles. Notably, although the initial cycles exhibited coulombic efficiencies slightly higher than 100% due to the activation of the Cu current collector, the CE quickly stabilized as cycling progressed. After the activation period, the average coulombic efficiency calculated from cycle 101 to cycle 9000 reached 100.604%, demonstrating highly reversible Zn plating/stripping behavior over extended cycling. Furthermore, the voltage fluctuations were significantly reduced for the 0.8GQDs@PVA@Zn system, indicating improved zinc reaction kinetics (Fig. S27 and 28, SI).

Cyclic voltammetry (CV) revealed that the Zn||Cu battery using 0.8GQDs@PVA@Zn and bare PVA@Zn showed similar redox peaks, suggesting that the inert GQDs did not participate in electrochemical reactions (Fig. S29, SI). Notably, during the first five cycles, the CV curves of 0.8GQDs@PVA@Zn showed stronger redox peak intensities with consistent shapes, indicating faster Zn^{2+} reaction kinetics and enhanced electrochemical reversibility (Fig. S30 and 31, SI). The zinc foil, ammonium vanadate (NVO), and hydrogel electrolyte were further assembled into a full-cell configuration for performance testing. The cyclic voltammetry (CV) curves of the full cell are shown in Fig. S32 (SI). It is evident that 0.8GQDs@PVA@Zn and bare PVA@Zn exhibit similar redox peaks, further confirming that the electrochemically inert GQDs do not participate in the electrochemical reaction. However, the full cells using 0.8GQDs@PVA@Zn exhibited higher peak intensities and smaller redox peak voltage differences, indicating improved capacity and reversibility. Furthermore, monitoring the capacity decay of the fully charged full-cell within 24 hours (Fig. S33 and 34, SI) showed that the full cell with 0.8GQDs@PVA@Zn retained 93.39% of its initial capacity, compared to 89.52% for bare PVA@Zn, demonstrating effective suppression of side reactions. Full-cell cycling performance at 3 A g^{-1} (Fig. 3g) revealed that the full cell with bare PVA@Zn exhibited a discharge capacity of only 116.9 mAh g^{-1} after 2000 cycles, with a capacity retention of 46.9%. In contrast, the full cell with 0.8GQDs@PVA@Zn maintained a discharge capacity of 221.2 mAh g^{-1}, with a capacity retention of 81.8%. At 1 A g^{-1}, 0.8GQDs@PVA@Zn also demonstrated more stable cycling performance (Fig. S35, SI). Rate performance testing at current densities ranging from 0.5 to 4 A g^{-1} (Fig. 3h, S36 and 37, SI) further confirmed the superior kinetics and cycling stability of 0.8GQDs@PVA@Zn. Even at a high current density of 4 A g^{-1}, the full cell with 0.8GQDs@PVA@Zn delivered a discharge capacity of 264.6 mAh g^{-1}, while bare PVA@Zn exhibited much lower discharge capacities at all tested current densities. The capacity of bare PVA@Zn rapidly declined upon returning to a lower current density, indicating slow Zn^{2+} diffusion kinetics and severe side reactions at the interface.

Finally, pouch cells assembled with 0.8GQDs@PVA@Zn demonstrated excellent electrochemical and mechanical stability. The pouch cell was fabricated using a 3.0 × 3.0 cm Ti foil-supported cathode (loading: 9.6 mg), a 3.5 × 3.5 cm Zn foil (50 μm thick) as the anode, and a 4.0 × 4.0 cm hydrogel electrolyte sheet. As shown in Fig. 3i, the pouch cell retained 90.6% of its initial capacity after 200 cycles at 0.2 A g^{-1}, confirming the robustness of the hydrogel electrolyte under practical operating conditions. These pouch cells also powered an LED light under various extreme conditions. As illustrated in Fig. 3j, the LED continued to operate even after folding the battery at 90° and 180° or cutting a portion of the battery, showcasing the excellent electrochemical and mechanical stability of 0.8GQDs@PVA@Zn. Furthermore, as shown in Fig. 3k, the pouch cell assembled with 0.8GQDs@PVA@Zn remained operational after being placed in ice and liquid nitrogen, confirming their excellent antifreeze properties. Additionally, as shown in Fig. 3l, the pouch cell also demonstrated exceptional pressure resistance. These results demonstrate that the modification of PVA hydrogels with GQDs significantly enhances the electrochemical and mechanical properties of the resulting electrolyte, making it a promising candidate for high-performance ZIBs under various harsh conditions.

SEI analysis

During the continuous charge–discharge cycles of zinc-ion batteries, an SEI film is formed between the zinc electrode and the hydrogel electrolyte due to side reactions. The thickness and composition of this film have a significant impact on the zinc ion transport rate and deposition behavior at the interface.[51] As shown in Fig. 4a, the SEI characteristics of Zn||Zn symmetric cells assembled with 0.8GQDs@PVA@Zn and bare PVA@Zn were analyzed after 10 cycles at a current density of 1 mA cm^{-2} using time-of-flight secondary ion mass spectrometry (TOF-SIMS). The zinc electrode in the bare PVA@Zn cell exhibited a higher concentration of fluoride ions (F^-) compared to the 0.8GQDs@PVA@Zn cell. These F^- ions are derived from the decomposition of $CF_3SO_3^-$ in the electrolyte under high voltage.[60] The presence of GQDs on the PVA matrix in 0.8GQDs@PVA@Zn enhances the fast conduction of zinc ions, which reduces polarization voltage and suppresses the side reactions, leading to a less intense F^- signal in the SEI of 0.8GQDs@PVA@Zn. The spatial distribution of F^- across the SEI layer also shows significant differences between the two systems. F^- in the SEI of the bare PVA@Zn system is concentrated near the zinc electrode side, whereas in the 0.8GQDs@PVA@Zn system, F^- is primarily located closer to the hydrogel electrolyte side, forming a thinner layer. Furthermore, the F^- concentration near the SEI surface facing the hydrogel electrolyte is lower in the 0.8GQDs@PVA@Zn system, as corroborated by the corresponding top-view mapping images (Fig. S38, SI). Additionally, three-dimensional visualization

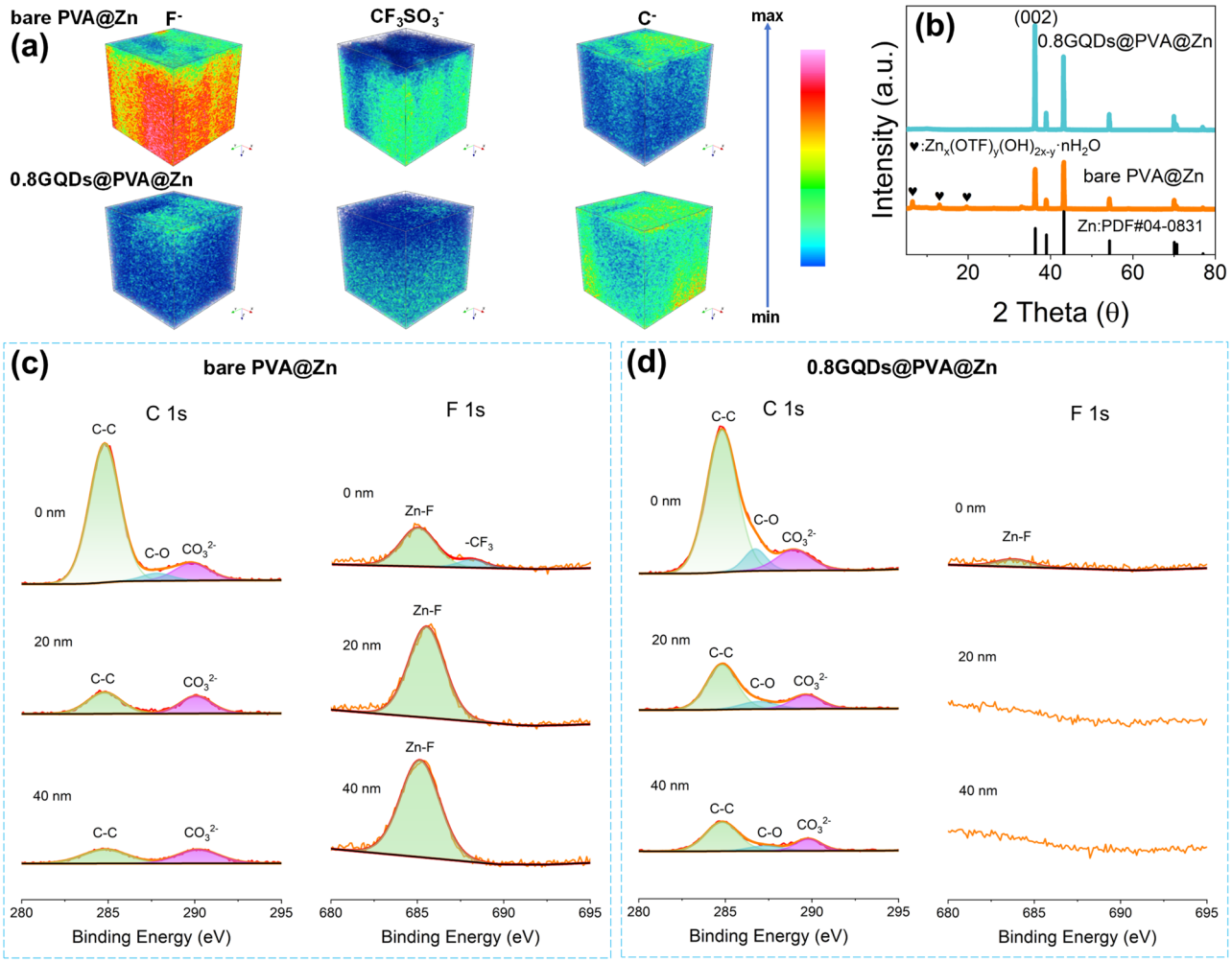

Fig. 4 Comparison of SEI composition and distribution on the zinc anode surface using different hydrogel electrolytes. (a) 3D visualization of TOM-SIMS depicting F^-, $CF_3SO_3^-$ and C^- signals. (b) XRD patterns after cycling tests at 1 mA cm^{-2}. XPS depth profile for C 1s and F 1s of the Zn anode surface with bare PVA@Zn (c) and 0.8GQDs@PVA@Zn (d).

using TOM-SIMS and top-view mapping (Fig. S39, SI) reveals a stronger $CF_3SO_3^-$ signal in the SEI of the bare PVA@Zn system, originating from side products such as $Zn_x(OTF)_y(OH)_{2x-y}\cdot nH_2O$,[61] which form due to the hydrogen evolution reaction between zinc and water. The introduction of GQDs into the PVA matrix reduces the reactivity of water molecules by interacting with them, thereby suppressing side reactions. Interestingly, the three-dimensional spatial distribution of carbon (C) and the two-dimensional top-view map display contrasting results (Fig. S40, SI). The SEI formed on zinc electrodes from the 0.8GQDs@PVA@Zn system contains a higher concentration of carbon compared to the bare PVA@Zn system. This seemingly contradicts the ability of 0.8GQDs@PVA@Zn to suppress side reactions. However, the carbon in the SEI may not solely originate from electrolyte decomposition or side products of the hydrogen evolution reaction. It could also arise from unreacted GQDs in the 0.8GQDs@PVA@Zn system. The esterification between GQDs and PVA is a reversible reaction, and some GQDs may remain non-covalently bonded to the PVA backbone through hydrogen bonds or interact with water molecules in the hydrogel electrolyte. Furthermore, GQDs are known to co-deposit with Zn^{2+} on the zinc electrode,[37] leading to the observed carbon distribution in the SEI. To verify this hypothesis, we performed confocal laser scanning tests on the cycled zinc electrodes. As shown in Fig. S41 (SI), the zinc electrode assembled with 0.8GQDs@PVA@Zn exhibited noticeable fluorescence signals, indicating that GQDs co-deposited with Zn^{2+} on the zinc surface. We further examined the cycled zinc electrodes *via* XRD analysis (Fig. 4b). The XRD patterns revealed a distinct peak corresponding to $Zn_x(OTF)_y(OH)_{2x-y}\cdot nH_2O$ in the bare PVA@Zn system, which was absent in the 0.8GQDs@PVA@Zn system, confirming that the GQD modification effectively suppressed the side reactions. Notably, the zinc electrode in the 0.8GQDs@PVA@Zn system exhibited a stronger (002) peak, indicating a more corrosion-resistant and compact zinc deposition along the (002) plane.[57]

We also performed XPS depth profiling to further investigate the composition and distribution of the SEI layer. As shown in Fig. 4c and d, the carbon content at 0 nm, 20 nm, and 40 nm

depths was higher in the 0.8GQDs@PVA@Zn system than in the bare PVA@Zn system. At depths of 20 nm and 40 nm, carbon peaks corresponding to C–O bonds were detected in the 0.8GQDs@PVA@Zn system, while these peaks were absent in the bare PVA@Zn system. C–O bonds originate from hydroxyl or ether groups on GQDs, further suggesting the incorporation of GQDs in the SEI. On the other hand, peaks corresponding to $ZnCO_3$ were more pronounced in the bare PVA@Zn system at 20 nm and 40 nm, further demonstrating the superior suppression of side reactions in the 0.8GQDs@PVA@Zn system. At 0 nm, the carbon peaks observed in both systems were attributed to the adhesion and residue of the PVA polymer on the zinc surface. Additionally, the F element data obtained from XPS etching highlighted a significant difference between the two systems. In the 0.8GQDs@PVA@Zn system, no fluoride peaks were detected at 20 nm and 40 nm, whereas the bare PVA@Zn system exhibited strong ZnF peaks at these depths. The bare PVA@Zn system also showed a peak at 0 nm corresponding to $-CF_3$ in $Zn_x(OTF)_y(OH)_{2x-y}\cdot nH_2O$, which was absent in the 0.8GQDs@PVA@Zn system. As shown in Fig. S42 (SI), the comparison of F element content obtained from Electron Probe Microanalysis (EPMA) is consistent with the results of the XPS depth profiling. In summary, through TOM-SIMS, XRD, and XPS depth profiling, we have confirmed the suppression of side reactions by 0.8GQDs@PVA@Zn and its role in modulating the composition and distribution of the SEI layer.

Zinc anode morphology observation and theoretical calculations

To further investigate the modulation effect of 0.8GQDs@PVA@Zn on zinc anode deposition behavior, the surface morphology of the zinc anode after cycling was observed using SEM. As shown in Fig. 5a and S43 (SI), the zinc anodes in batteries assembled with bare PVA@Zn and 0.8GQDs@PVA@Zn exhibited significant differences in surface morphology after cycling for 10, 20, and 40 cycles at a current density of 1.0 mA cm^{-2}. After 10 cycles, numerous plate-like dendrites were observed growing vertically on the surface of the zinc anode with bare PVA@Zn, and the cross-sectional SEM image revealed a layer of loose and uneven zinc metal deposition on the zinc plate. After 40 cycles, the plate-like dendrites had grown larger, and the cross-section showed that the surface of the zinc plate had transitioned from uneven small protrusions to well-formed dendrites. Moreover, the interior of the zinc plate exhibited corrosion-induced voids due to side reactions. In contrast, the surface of the zinc anode with 0.8GQDs@PVA@Zn was much smoother and more uniform, with no prominent dendrite formation, and the deposited layer was denser, with no noticeable protrusions or voids inside the zinc plate. To visually demonstrate the guiding role of 0.8GQDs@PVA@Zn in zinc ion deposition, *in situ* optical microscopy was used to monitor the morphological changes of zinc deposition in real time. As shown in Fig. S44 (SI), after 5 minutes of initial deposition, an irregular and uneven surface with protrusions was observed on the zinc anode with bare PVA@Zn. With increasing deposition time to 10 minutes, due to continued two-dimensional diffusion and the tip effect, zinc ions further aggregated to form protrusions, which then evolved into disordered dendrites. In contrast, the deposition on the 0.8GQDs@PVA@Zn anode remained flat and compact, with no dendrite formation, visually indicating that GQD modification of the hydrogel created more nucleation sites, thus inhibiting dendrite growth. Furthermore, after 20 cycles of the Zn‖Zn symmetric cell at 1 mA cm^{-2}, optical microscopy images and corresponding three-dimensional height distribution simulations (Fig. 5b–e and S45, SI) clearly show an uneven surface and large zinc agglomerates on the zinc anode with bare PVA@Zn, further confirming the rough surface and protruding dendrites. After introducing 0.8GQDs@PVA@Zn, the zinc ions exhibited completely different deposition behavior, depositing along the direction parallel to the zinc substrate rather than continuing vertical accumulation. The corresponding three-dimensional height simulations also showed significantly lower values compared to bare PVA@Zn.

Finite element simulations were employed to study the zinc ion flux on the zinc anode surface. As shown in Fig. 5f, on the surface of the bare PVA@Zn anode, zinc ions are transported within the three-dimensional polymeric pores of the hydrogel to the zinc plate surface, forming initial nucleation sites located in the center of polymer channels. The tip effect creates an uneven electric field, leading to localized Zn^{2+} concentration polarization, where the tips serve as charge-rich centers, driving further ion aggregation at the initial nucleation sites and ultimately evolving into dendrites. In stark contrast, when quantum-sized GQDs are incorporated into the PVA polymer matrix, due to the complexation between GQDs and Zn^{2+}, Zn^{2+} ions are transported along the GQDs, which reduces the Zn^{2+} flux in the polymeric channels and weakens Zn^{2+} accumulation at the tips (Fig. 5g). Additionally, under the guidance of GQDs, zinc ions nucleate not only in the middle of the polymeric channels but also near the GQDs, generating more nucleation sites and suppressing dendrite growth. Moreover, the electric field distribution simulation on the zinc anode surface showed that the electrode surface with 0.8GQDs@PVA@Zn exhibited a relatively uniform electric field distribution, which is primarily attributed to the GQDs promoting the formation of abundant nucleation sites, allowing Zn^{2+} to adsorb evenly across the entire electrode, thereby inducing uniform nucleation (Fig. S46, SI). Subsequently, density functional theory (DFT) calculations were employed to investigate the interaction between the zinc-affinitive groups on the GQD surface and Zn^{2+} (Fig. S47 and 48, SI). Due to the weak adsorption between Zn^{2+} and the zinc substrate, limited nucleation sites and sustained lateral two-dimensional diffusion result in zinc ions continuously depositing in the initially limited nucleation regions, ultimately growing into dendrites.[30] As shown in Fig. 5h, the adsorption energies of ether, hydroxyl, and carboxyl groups on the GQD surface for Zn^{2+} were much higher than the binding energies between Zn^{2+} and the bridge and top sites on Zn(100) and Zn(001) crystal planes, indicating that GQDs have a stronger affinity for Zn, which facilitates the reduction of nucleation barriers and increases the number of nucleation sites. The

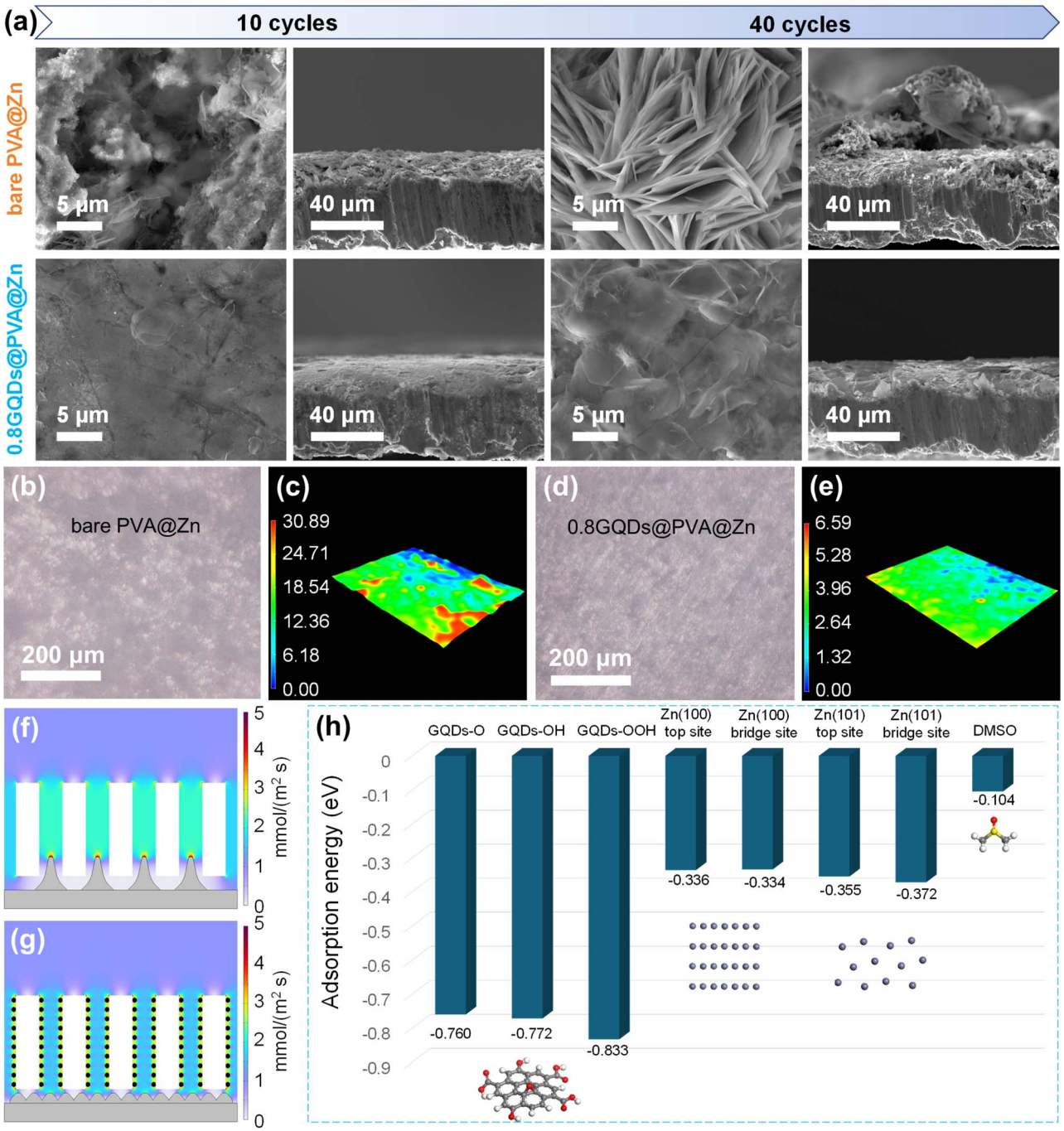

Fig. 5 Observation of zinc anode deposition and theoretical calculations. (a) Surface and cross-sectional SEM images of the Zn anode after different cycles in the Zn||Zn symmetric cell. Optical microscope images (b and d) and corresponding height distribution (c and e) of Zn foil. Simulation of the Zn^{2+} concentration gradient during deposition on the Zn anode based on bare PVA@Zn (f) and 0.8GQDs@PVA@Zn (g). (h) Adsorption energy of Zn ion on Zn, DMSO and different oxygen-function groups of GQDs.

calculations also showed that GQDs have a higher affinity for Zn^{2+} than the DMSO contained in the hydrogel system, meaning that after DMSO enters the solvent structure of $[Zn(H_2O)_6]^{2+}$, the introduction of GQDs remodels this solvation structure. Through the morphology observation of the zinc anode surface and theoretical calculations, it is concluded that 0.8GQDs@PVA@Zn can form a uniform electric field distribution, homogenize the Zn^{2+} flux, guide the formation of more nucleation sites, and effectively suppress dendrite formation.

Conclusions

In summary, uniform-sized, single-layer GQDs with high yield were successfully prepared using spent graphite from retired

lithium-ion batteries as raw material. By anchoring the obtained GQDs onto PVA chains through chemical bonding, a hydrogel electrolyte with exceptional mechanical and electrochemical performance was developed. The Zn||Zn symmetric battery assembled using 0.8GQDs@PVA@Zn demonstrated stable operation for 5500 hours, while the Zn||Cu half-cell exhibited extraordinary cycling stability over 9000 cycles. Furthermore, the assembled pouch cells not only maintained energy output at low temperatures but also retained stable operation after bending, shearing, and compression. Analysis of the SEI composition revealed that the modification of the hydrogel electrolyte by GQDs effectively suppressed two major side reactions in the system and optimized the composition and distribution of the SEI. Additionally, finite element simulations and DFT calculations synergistically elucidated the mechanism by which GQDs stabilize the zinc anode by homogenizing the Zn^{2+} flux. This study provides a high-value utilization strategy for the recycling of spent graphite from lithium-ion batteries and develops a feasible approach for the preparation of high-quality and high-yield GQDs. Moreover, it expands the application of GQDs in hydrogel electrolytes for zinc-ion batteries.

Author contributions

Dingzhong Luo: investigation and writing – original draft. Yinger Xiang: investigation. Zhenglei Geng: investigation. Huaxin Liu: investigation. Xue Zhong: investigation. Zhi Zheng: investigation. Zhiyu Hu: investigation. Shengli Lu: investigation. Wentao Deng: investigation. Guoqiang Zou: investigation. Xiaobo Ji: methodology, supervision, funding acquisition, and writing – review & editing. Hongshuai Hou: methodology, supervision, funding acquisition, and writing – review & editing.

Conflicts of interest

There are no conflicts to declare.

Data availability

The data that support the findings of this study are available from the corresponding author upon reasonable request.

Supplementary Information (SI): includes detailed descriptions of hydrogel electrolyte preparation, electrochemical measurements, and computational methods. See DOI: https://doi.org/10.1039/d5sc08142d.

Acknowledgements

This work was financially supported by the National Natural Science Foundation of China (22379165, 52074359, U21A20284, and U22B2069) and the Fundamental Research Funds for the Central Universities of Central South University (2024ZZTS0389).

Notes and references

1 B. K. Biswal, B. Zhang, P. Thi Minh Tran, J. Zhang and R. Balasubramanian, *Chem. Soc. Rev.*, 2024, **53**, 5552–5592.
2 N. Ogihara, K. Nagaya, H. Yamaguchi, Y. Kondo, Y. Yamada, T. Horiba, T. Baba, N. Ohba, S. Komagata, Y. Aoki, H. Kondo, T. Sasaki and S. Okayama, *Joule*, 2024, **8**, 1364–1379.
3 J. Wang, J. Ma, Z. Zhuang, Z. Liang, K. Jia, G. Ji, G. Zhou and H.-M. Cheng, *Chem. Rev.*, 2024, **124**, 2839–2887.
4 Y. Guo, Y. Li, K. Qiu, Y. Li, W. Yuan, C. Li, X. Rui, L. Shi, Y. Hou, S. Liu, D. Ren, T. Tan, G. Zhu, L. Lu, S. Xu, B. Deng, X. Liu and M. Ouyang, *Energy Environ. Sci.*, 2025, **18**, 264–274.
5 S.-J. Han, L. Xu, C. Chen, Z.-Y. Wang, M.-L. Fu and B. Yuan, *Sep. Purif. Technol.*, 2024, **330**, 125289.
6 S. Xie, Y. Dong, X. Wang, Z. Zeng, H. Zhou, Z. Yuan, W. Sun, X. Ji, Y. Yang and P. Ge, *Energy Storage Mater.*, 2024, **70**, 103510.
7 M. Shan, S. Xu, Y. Cao, B. Han, X. Zhu, T. Zhang, C. Dang, J. Zhu, Q. Zhou, Z. Xue, Y. Xu, Q. Zhu, M. S. Islam, B. H. Yin, X. Chang, C. Cao, G. Xu and M. Zhu, *Adv. Funct. Mater.*, 2024, **34**, 2411834.
8 H. Tian, M. Graczyk-Zajac, A. Kessler, A. Weidenkaff and R. Riedel, *Adv. Mater.*, 2023, **36**, 2308494.
9 Z. Ge, A. M. Graf, J. Keski-Rahkonen, S. Slizovskiy, P. Polizogopoulos, T. Taniguchi, K. Watanabe, R. Van Haren, D. Lederman, V. I. Fal'ko, E. J. Heller and J. Velasco, *Nature*, 2024, **635**, 841–846.
10 Z. Ge, S. Slizovskiy, P. Polizogopoulos, T. Joshi, T. Taniguchi, K. Watanabe, D. Lederman, V. I. Fal'ko and J. Velasco, *Nat. Nanotechnol.*, 2023, **18**, 250–256.
11 W. Liu, M. Li, G. Jiang, G. Li, J. Zhu, M. Xiao, Y. Zhu, R. Gao, A. Yu, M. Feng and Z. Chen, *Adv. Energy Mater.*, 2020, **10**, 2001275.
12 K. Wu, Y. Wang, Y. Wan, W. Gu, L. Zhang, X. Yang, S. Chou, H. K. Liu, S. X. Dou and C. Wu, *Adv. Funct. Mater.*, 2024, **35**, 2412027.
13 H. Yan, Q. Wang, J. Wang, W. Shang, Z. Xiong, L. Zhao, X. Sun, J. Tian, F. Kang and S. H. Yun, *Adv. Mater.*, 2023, **35**, 2210809.
14 H. Liu, Z. Deng, Z. Zhang, W. Lin, M. Zhang and H. Wang, *Matter*, 2024, **7**, 977–990.
15 C. Xia, Y. Qiu, Y. Xia, P. Zhu, G. King, X. Zhang, Z. Wu, J. Y. Kim, D. A. Cullen, D. Zheng, P. Li, M. Shakouri, E. Heredia, P. Cui, H. N. Alshareef, Y. Hu and H. Wang, *Nat. Chem.*, 2021, **13**, 887–894.
16 L. Ye, M. Liao, X. Cheng, X. Zhou, Y. Zhao, Y. Yang, C. Tang, H. Sun, Y. Gao, B. Wang and H. Peng, *Angew. Chem., Int. Ed.*, 2021, **60**, 17419–17425.
17 P. Tian, L. Tang, K.-S. Teng and S.-P. Lau, *Mater. Futures*, 2024, **3**, 022301.
18 S. Chung, R. A. Revia and M. Zhang, *Adv. Mater.*, 2021, **33**, 1904362.
19 D. Medina-Lopez, T. Liu, S. Osella, H. Levy-Falk, N. Rolland, C. Elias, G. Huber, P. Ticku, L. Rondin, B. Jousselme,

D. Beljonne, J.-S. Lauret and S. Campidelli, *Nat. Commun.*, 2023, **14**, 4728.
20 L. Shi, B. Wang and S. Lu, *Matter*, 2023, **6**, 728–760.
21 T. Zhao, K. Wang, F. Liu, S. Zhang and S.-H. Ho, *Chin. Chem. Lett.*, 2024, 110321.
22 Y. Yan, J. Gong, J. Chen, Z. Zeng, W. Huang, K. Pu, J. Liu and P. Chen, *Adv. Mater.*, 2019, **31**, 1808283.
23 R. Ye, C. Xiang, J. Lin, Z. Peng, K. Huang, Z. Yan, N. P. Cook, E. L. G. Samuel, C.-C. Hwang, G. Ruan, G. Ceriotti, A.-R. O. Raji, A. A. Martí and J. M. Tour, *Nat. Commun.*, 2013, **4**, 2943.
24 J. Cai, G. Han, J. Ren, C. Liu, J. Wang and X. Wang, *Chem. Eng. J.*, 2022, **435**, 131833.
25 Y. Qiao, H. Zhao, Y. Shen, L. Li, Z. Rao, G. Shao and Y. Lei, *EcoMat*, 2023, **5**, 12321.
26 S. Weng, S. Wu, Z. Liu, G. Yang, X. Liu, X. Zhang, C. Zhang, Q. Liu, Y. Huang, Y. Li, M. N. Ateş, D. Su, L. Gu, H. Li, L. Chen, R. Xiao, Z. Wang and X. Wang, *Carbon Energy*, 2022, **5**, 224.
27 Q. Li, D. Luo, Q. Ma, Z. Zheng, S. Li, Y. Xie, L. Xue, M. Lin, Y. Nie, G. Feng, H. Dou, J. Chen, X. Wang and Z. Chen, *Energy Environ. Sci.*, 2025, **18**, 1489–1501.
28 Z. Zhang, T. Xu, K. Xu, Z. Jiang, D. Sun, C. Wang, J. Feng, B. Xi and S. Xiong, *Angew. Chem., Int. Ed.*, 2025, 202424272.
29 H. Wang, A. Zhou, X. Hu, Z. Hu, F. Zhang, Y. Huang, L. Li, F. Wu and R. Chen, *ACS Nano*, 2023, **17**, 11946–11956.
30 W. Han, H. Lee, Y. Liu, Y. Kim, H. Chu, G. Liu and W. Yang, *Chem. Eng. J.*, 2023, **452**, 139090.
31 S.-J. Guo, M.-Y. Yan, D.-M. Xu, P. He, K.-J. Yan, J.-X. Zhu, Y.-K. Yu, Z.-Y. Peng, Y.-Z. Luo and F.-F. Cao, *Energy Environ. Sci.*, 2025, **18**, 418–429.
32 S. Yang, Q. Wu, Y. Li, F. Luo, J. Zhang, K. Chen, Y. You, J. Huang, H. Xie and Y. Chen, *Angew. Chem., Int. Ed.*, 2024, **63**, e202409160.
33 H. Tian, M. Yao, Y. Guo, Z. Wang, D. Xu, W. Pan and Q. Zhang, *Adv. Energy Mater.*, 2024, 2403683.
34 Y. Guo, J. Bae, Z. Fang, P. Li, F. Zhao and G. Yu, *Chem. Rev.*, 2020, **120**, 7642–7707.
35 Y. Yan, S. Duan, B. Liu, S. Wu, Y. Alsaid, B. Yao, S. Nandi, Y. Du, T. W. Wang, Y. Li and X. He, *Adv. Mater.*, 2023, **35**, 2211673.
36 Y. Zhang, X. Jing, J. Zou, P. Feng, G. Wang, J. Zeng, L. Lin, Y. Liu, H. Y. Mi and S. Nie, *Adv. Funct. Mater.*, 2024, **34**, 2410698.
37 H. Zhang, R. Guo, S. Li, C. Liu, H. Li, G. Zou, J. Hu, H. Hou and X. Ji, *Nano Energy*, 2022, **92**, 106752.
38 Y. Hu, W. Chen, T. Lei, Y. Jiao, H. Wang, X. Wang, G. Rao, X. Wang, B. Chen and J. Xiong, *Nano Energy*, 2020, **68**, 104373.
39 S. Yang, J. Sun, X. Li, W. Zhou, Z. Wang, P. He, G. Ding, X. Xie, Z. Kang and M. Jiang, *J. Mater. Chem. A*, 2014, **2**, 8660–8667.
40 W. Fu, J. Yin, H. Cao, Z. Zhou, J. Zhang, J. Fu, J. H. Warner, C. Wang, X. Jia, G. N. Greaves and A. K. Cheetham, *Adv. Mater.*, 2023, **35**, 2304074.
41 S. Wu, Y. Alsaid, B. Yao, Y. Yan, Y. Zhao, M. Hua, D. Wu, X. Zhu and X. He, *EcoMat*, 2021, **3**, 12085.
42 Q. He, Z. Chang, Y. Zhong, S. Chai, C. Fu, S. Liang, G. Fang and A. Pan, *ACS Energy Lett.*, 2023, **8**, 5253–5263.
43 S. Sangngern, S. Sahasithiwat, A. Kaewvilai, N. Koonsaeng and A. Laobuthee, *Sens. Actuators, B*, 2011, **156**, 961–968.
44 Y. Wu, T. Liu, Y. Shi and H. Wang, *Polymer*, 2022, **249**, 124842.
45 T. Liu, X. Peng, Y. Chen, J. Zhang, C. Jiao and H. Wang, *Polym. Chem.*, 2020, **11**, 4787–4797.
46 D. H. Lee, Y. H. Song, H. J. Ahn, J. Lee and H. C. Woo, *Molecules*, 2024, **29**, 4807.
47 X. Liang, H.-J. Zhong, H. Ding, B. Yu, X. Ma, X. Liu, C.-M. Chong and J. He, *Polymers*, 2024, **16**, 2755.
48 K. Leng, G. Li, J. Guo, X. Zhang, A. Wang, X. Liu and J. Luo, *Adv. Funct. Mater.*, 2020, **30**, 2001317.
49 C. Fu, Y. Wang, C. Lu, S. Zhou, Q. He, Y. Hu, M. Feng, Y. Wan, J. Lin, Y. Zhang and A. Pan, *Energy Storage Mater.*, 2022, **51**, 588–598.
50 J. Liu, Z. Khanam, S. Ahmed, T. Wang, H. Wang and S. Song, *ACS Appl. Mater. Interfaces*, 2021, **13**, 16454–16468.
51 Q. He, G. Fang, Z. Chang, Y. Zhang, S. Zhou, M. Zhou, S. Chai, Y. Zhong, G. Cao, S. Liang and A. Pan, *Nano-Micro Lett.*, 2022, **14**, 93.
52 H. Zhang, X. Gan, Y. Gao, H. Wu, Z. Song and J. Zhou, *Adv. Mater.*, 2024, **37**, 2411997.
53 S. Huang, L. Hou, T. Li, Y. Jiao and P. Wu, *Adv. Mater.*, 2022, **34**, 2110140.
54 Y. Wang, Q. Li, H. Hong, S. Yang, R. Zhang, X. Wang, X. Jin, B. Xiong, S. Bai and C. Zhi, *Nat. Commun.*, 2023, **14**, 3890.
55 J. Kang, Z. Jiang and L. Wen, *Adv. Funct. Mater.*, 2025, 2422566.
56 J. Li, H. Zhang, Z. Liu, H. Du, H. Wan, X. Li, J. Yang and C. Yan, *Adv. Funct. Mater.*, 2024, **35**, 2412865.
57 F. Luo, S. Yang, Q. Wu, Y. Li, J. Zhang, Y. Zhang, J. Huang, H. Xie and Y. Chen, *Energy Environ. Sci.*, 2024, **17**, 8570–8581.
58 Y. Xiong, H. Cheng, Y. Jiang, Z. Fan, X. Li, G. Wang, T. Liu and X. Gu, *Energy Storage Mater.*, 2025, **74**, 103981.
59 M. Chen, W. Zhou, A. Wang, A. Huang, J. Chen, J. Xu and C.-P. Wong, *J. Mater. Chem. A*, 2020, **8**, 6828–6841.
60 Y. Wu, Z. Zhu, D. Shen, L. Chen, T. Song, T. Kang, Z. Tong, Y. Tang, H. Wang and C. S. Lee, *Energy Storage Mater.*, 2022, **45**, 1084–1091.
61 S. Deng, Y. Sun, Z. Yang, M. Wu, H. Tong, X. Nie, Y. Su, J. Li and G. Chai, *Adv. Funct. Mater.*, 2024, **34**, 2408546.